International Journal of Heat and Mass Transfer 106 (2017) 708–719

Contents lists available at ScienceDirect

International Journal of Heat and Mass Transfer

journal homepage: www.elsevier.com/locate/ijhmt

Nucleate boiling performance evaluation of cavities at mesoscale level

Yu-Tong Mu [a], Li Chen [a], Ya-Ling He [a], Qin-Jun Kang [b], Wen-Quan Tao [a,*]

[a] Key Laboratory of Thermo-Fluid Engineering and Science of MOE, School of Energy and Power Engineering, Xi'an Jiaotong University, Xi'an, Shaanxi, 710049, China
[b] Computational Earth Science Group (EES-16), Los Alamos National Laboratory, Los Alamos, NM, USA

ARTICLE INFO

Article history:
Received 11 August 2016
Received in revised form 17 September 2016
Accepted 18 September 2016
Available online 29 September 2016

Keywords:
Lattice Boltzmann method
Nucleate boiling
Conjugated heat transfer
Cavity shape
Multi-relaxation-time (MRT)

ABSTRACT

Nucleate boiling heat transfer (NBHT) from enhanced structures is an effective way to dissipate high heat flux. In the present study, a 3D multi-relaxation-time (MRT) phase-change lattice Boltzmann method in conjunction with conjugated heat transfer treatment is proposed and then applied to the study of cavities behaviours for nucleation on roughened surfaces for an entire ebullition cycle without introducing any artificial disturbance. The bubble departure diameter, departure frequency and total boiling heat transfer rate are also explored. It is demonstrated that the cavity shapes show significant influence on the features of NBHT. The total heat transfer rate increases with the cavity mouth and cavity base area while decreases with the increase in cavity bottom wall thickness. The cavity with low wetting can enhance the heat transfer and improve the bubble release frequency.

1. Introduction

The last century has witnessed a surge in boiling heat transfer research due to its complexity involving the thermal fluctuations at the molecular scale and convective motion and energy transport at the macroscopic scale [1–4]. Nucleate boiling heat transfer (NBHT) has been recognized as an effective mechanism for heat dissipation because of the latent heat accompanying the liquid–vapor transition [5]. Based on the fundamental physics of different mechanisms of nucleation, the homogeneous, heterogeneous, pseudo-classical as well as non-classical nucleations have been proposed [6,7]. However, they do not offer a comprehensive understanding of the important features in NBHT such as the bubble release frequency, bubble departure diameter and critical heat flux (CHF). Extensive empirical correlations with limited application range and several adjustable variables have thus been tailored for engineering needs [8–14].

With respect to boiling heat transfer enhancement, surface modification is considered to be implemented in a cost effective way when compared with the active methods such as the nanofluids and/or porous coating [8,15,16]. The first study in this regard was conducted by Jakob [17] who investigated the effect of surface roughness on boiling heat transfer. After that a large number of experimental studies on the surface characteristics have been conducted with the rapid growth in surface fabrication technologies [1]. As the microscopic scale is concerned, almost all the surfaces in nature are made up of many cavities and crevices. Those imperfections can serve as nucleation sites [18]. Heat transfer enhancements by such cavities are experimentally obtained with an improvement of heat transfer coefficient by eightfold times [11], CHF value by two-and half times [11], and incipient superheat decreasing by 80–90% [19]. The mechanisms on the heat transfer augmentation may be attributed to the increasing mobility of the vapor liquid surface [20] or the lowering interfacial free energy of the nucleus [3].

Experimental results show that the activation density is determined by the wall superheat, heat flux, surface wettability and cavity geometry [18,21,22]. It is suggested that the initial boiling superheat needed and its stability are influenced by the cavity mouth diameter and shape, respectively [23]. The cavity depth could result in premature rapid decline of overall heat transfer performance due to the larger flow resistance for the rewetting of liquid [24]. However, the activation of the cavity can also turn to be inactive because of the interactions among bubbles, which has been investigated firstly by Chekanov [25]. Three types of bubble coalescences including the vertical, horizontal and declining bubble coalescence have been proposed based on the ratio of the cavity spacing to the average bubble departure diameter [26]. Although a wide variety of cavities are designed and experimentally investigated by researchers, no one can expect to answer the question on what kind of micro-structured cavity performs the best performance of NBHT [7] to maximize heat transfer from solid to fluid?

* Corresponding author.
E-mail address: wqtao@mail.xjtu.edu.cn (W.-Q. Tao).

http://dx.doi.org/10.1016/j.ijheatmasstransfer.2016.09.058
0017-9310/

With the development of computer technology, numerical simulations on NBHT have received much attention. Studies of direct numerical simulation on boiling were mostly reported at macroscopic scale where several kinds of interface tracking methods were used, such as VOF, level-set and VOSET methods [27]. However, with these methods, an initial nucleate embryo and a waiting period should be assigned, and thus they cannot describe the entire ebullition of the bubble cycles. With a number of molecular particles introduced in a system at microscopic scale, molecular dynamics simulations were performed in a natural and comprehensive manner without any artificial assumption [28]. However, the simulations are limited to a very small size. Lattice Boltzmann method (LBM), as a mesoscopic method based on the discrete kinetic theory, has been widely applied for the boiling heat transfer when coupled with some thermal models [29–36]. Three boiling stages of pool boiling are reproduced by Gong and Cheng [36] and Li et al. [31]. Some effects of cavity geometry and wall wettability on the bubble departure diameter and bubble release frequency are also explored [33,34,36]. However, there are still some deficiencies involving the treatment of nucleation formation and the thermal models. For the treatment of nucleation formation, Márkus and Házi [34] initially assigned an existing embryo in their work, which cannot reflect the entire ebullition cycle. Li et al. [31] and Zhang and Chen [35] added small temperature fluctuations in the grid, which is equivalent to adding a density disturbance according to the equation of state. It is our understanding that any non-uniformity, including those in surface wettability, wall temperature or heat flux distribution, surface roughness, etc., can serve as a disturbance to promote the nucleation. And all these non-uniformities are problem inherent characteristics, hence, are more reasonable and acceptable. Therefore the practice of setting a high temperature point on the heating wall to stimulate nucleation can be removed. As for the treatment of thermal models, two aspects may be mentioned. First is the thermodynamic equation of state. The equation of state adopted in the model of Márkus and Házi [33,34] was not for real gases. Second is the conjugated condition treatment of the heating wall. The importance of the conjugated heat transfer treatment for the heating wall has been addressed in [29,37]. However, in some papers published a bit earlier this treatment was often ignored, leading to an application limitation to the steady-state solutions when the thermal conductivities of different components are identical [38].

Herein, we present an improved thermal model considering the conjugated heat transfer in a solid-fluid system. The model is applied on the cavity behaviour for nucleation on roughened surface for the entire ebullition cycle without introducing any artificial disturbance. The outline of the rest of the paper is as follows. Section 2 gives a brief introduction to the multiphase flow model together with the improved thermal model. In Section 3, some numerical tests are performed to validate the present model. In Section 4, we investigate the detailed embryo nucleation and the entire ebullition process, and then the effects of cavity configuration, base area, solid thickness and wall wettability are explored and discussed. Section 5 provides some conclusions.

2. Lattice Boltzmann method

2.1. The pseudo-potential MRT approach for multiphase flow

In the multi-relaxation-time (MRT) collision method, a higher numerical stability and lower spurious velocity can be achieved by choosing different separated time scales to represent changes in the various physical processes. The motion of the fluid described by a set of density distribution functions is considered as a collective behavior of pseudo-particles at a mesoscopic level [39,40]. The evolution of the standard LB equation with MRT collision is expressed as follows [41]:

$$f_\alpha(\boldsymbol{x}+\boldsymbol{e}_\alpha\delta t, t+\delta t) = f_\alpha(\boldsymbol{x},t) - \sum_\beta \Omega_{\alpha\beta}(f_\beta(\boldsymbol{x},t) - f_\beta^{eq}(\boldsymbol{x},t)) + \sum_\beta (\mathrm{I}_{\alpha\beta} - 0.5\Omega_{\alpha\beta})S_\beta(\boldsymbol{x},t) \quad (1)$$

where $f_\alpha(\boldsymbol{x}, t)$ is the density distribution function at the lattice site $\boldsymbol{x}$ and time t, f_β^{eq} is the equilibrium distribution in the βth direction, Ω is the collision matrix, $\mathbf{I}$ is the identity matrix and $\boldsymbol{e}_\alpha$ is the particle velocity in the αth direction. For the three-dimensional nineteen-velocity (D3Q19) model, $\boldsymbol{e}_\alpha$ is expressed as follows:

$$\boldsymbol{e}_\alpha = \begin{cases} (0,0,0), & \alpha = 0 \\ (\pm1,0,0),(0,\pm1,0),(0,0,\pm1), & \alpha = 1,\ldots,6 \\ (\pm1,\pm1,0),(\pm1,0,\pm1),(0,\pm1,\pm1) & \alpha = 7,\ldots,18 \end{cases} \quad (2)$$

The forcing term S_α is related to the total force $\mathbf{F}$ as follows [42]

$$S_\alpha = w_\alpha\left[\frac{\boldsymbol{e}_\alpha - \mathbf{u}}{c_s^2} + \frac{\boldsymbol{e}_\alpha - \mathbf{u}}{c_s^4}\boldsymbol{e}_\alpha\right]\cdot\mathbf{F} \quad (3)$$

where $w_\alpha = 1/3$ for $\alpha = 0$, $w_\alpha = 1/18$ for $\alpha = 1$–6 and $w_\alpha = 1/36$ for $\alpha = 7$–18. $c_s = c/\sqrt{3}$, and c is the lattice sound speed.

With a transformation matrix $\mathbf{T}$, the right side of Eq. (1) can be mapped onto moment space as

$$\mathbf{m}^* = \mathbf{m} - \mathbf{\Lambda}(\mathbf{m} - \mathbf{m}^{eq}) + \delta_t(\mathbf{I} - 0.5\mathbf{\Lambda})\mathbf{S} \quad (4)$$

where $\mathbf{m}$ and $\mathbf{m}^{eq}$ are the moment space of the density distribution of $\mathbf{f}$ and $\mathbf{f}^{eq}$, which are derived from $\mathbf{m} = \mathbf{Tf}$ and $\mathbf{m}^{eq} = \mathbf{Tf}^{eq}$, respectively. The matrix $\mathbf{T}$ can be found in [41]. $\mathbf{m}^{eq}$ can be expressed as follows:

$$\mathbf{m}^{eq} = \rho\begin{pmatrix} 1, -11+19(u_x^2+u_y^2+u_z^2), 3-\frac{11}{2}(u_x^2+u_y^2+u_z^2), \\ u_x, -\frac{2}{3}u_x, u_y, -\frac{2}{3}u_y, u_z, -\frac{2}{3}u_z, \\ 2u_x^2-u_y^2-u_z^2, \frac{1}{2}(2u_x^2-u_y^2-u_z^2), u_y^2-u_z^2, \frac{1}{2}(u_y^2-u_z^2), \\ u_xu_y, u_yu_z, u_xu_z, 0, 0, 0 \end{pmatrix}^T \quad (5)$$

The diagonal matrix $\mathbf{\Lambda}$ is given by [43]

$$\mathbf{\Lambda} = \mathrm{diag}(s_0, s_e, s_\varepsilon, s_0, s_q, s_0, s_q, s_0, s_q, s_\nu, s_\pi, s_\nu, s_\pi, s_\nu, s_\nu, s_\nu, s_t, s_t, s_t) \quad (6)$$

Following the work presented in [42,44], the improved source term $\mathbf{S}$ to achieve thermodynamic consistency is given by

$$\mathbf{S} = \begin{cases} 0 \\ 38(u_xF_x+u_yF_y+u_zF_z) + \frac{114\varepsilon(F_x^2+F_y^2+F_z^2)}{\psi^2(1/s_e-0.5)} \\ -11(u_xF_x+u_yF_y+u_zF_z) \\ F_x \\ -2/3F_x \\ F_y \\ -2/3F_y \\ F_z \\ -2/3F_z \\ 2(2u_xF_x-u_yF_y-u_zF_z) \\ -2u_xF_x+u_yF_y+u_zF_z \\ 2(u_yF_y-u_zF_z) \\ -u_yF_y+u_zF_z \\ u_xF_y+u_yF_x \\ u_yF_z+u_zF_y \\ u_xF_z+u_zF_x \\ 0,\ 0,\ 0 \end{cases} \quad (7)$$

where ε is used to tune the mechanical stability and is selected as 0.09 in the present study. It is noted that the width of interface diffusion layer can somewhat be decreased by changing the parameter ε. The total force $\mathbf{F}$ acting on a fluid particle includes the fluid–fluid interaction force $\mathbf{F}_f$, fluid–solid interaction force $\mathbf{F}_s$ and other forces (such as the gravitational force $\mathbf{F}_g$). The interaction force is given by [30]

$$\mathbf{F}_f = -G_f\psi(\boldsymbol{x})c_s^2\sum_{\alpha=1}^{18} w(|\boldsymbol{e}_\alpha|^2)\psi(\boldsymbol{x}+\boldsymbol{e}_\alpha\delta_t)\boldsymbol{e}_\alpha \tag{8}$$

where G_f reflects the interaction strength among the fluid, and $w(|\boldsymbol{e}_\alpha|^2)$ are the weights. In the present study, only the interactions of six nearest neighbors and twelve next-nearest neighbors are considered. The effective mass $\psi(\boldsymbol{x})$ is defined to calculate the interaction force based on local fluid density

$$\psi(\boldsymbol{x}) = \sqrt{\frac{2(p-\rho c_s^2)}{G_f c_s^2}} \tag{9}$$

A non-ideal fluid with the P-R equation of state (EOS) is adopted [45]

$$p = \frac{\rho RT}{1-b\rho} - \frac{a\alpha(T)\rho^2}{1+2b\rho-b^2\rho^2} \tag{10}$$

with $\alpha(T) = \left[1+(0.37464+1.54226\omega-0.26992\omega^2)\times(1-\sqrt{T/Tc})\right]^2$, $a = 0.45724(RT_c)^2/p_c$, $b = 0.1873RT_c/p_c$. Substituting Eq. (10) to (9), the effective mass can be calculated. Note that G_f can be cancelled out and is put there only to ensure the right hand side of Eq. (9) to be reasonable. In order to simulate the nucleation process of water in the simulation, we choose $G_f = -1$, $a = 3/49$, $b = 2/21$, $R = 1$ and $\omega = 0.344$. The critical parameters in lattice units such as the critical pressure p_c, temperature T_c and density ρ_c are chosen as 0.089355, 0.109383 and 2.541858, respectively.

The fluid–solid force describing the wetting condition is given by [30]

$$\mathbf{F}_s = -G_s\psi(\boldsymbol{x})c_s^2\sum_{\alpha=1}^{18} w(|\boldsymbol{e}_\alpha|^2)l(\boldsymbol{x}+\boldsymbol{e}_\alpha\delta_t)\boldsymbol{e}_\alpha \tag{11}$$

where l is an indicator function that equals 0 for fluid nodes and equals 1 for solid nodes. G_s can be tuned to obtain different contact angles. It is noted that G_s is chosen as 0 without explicit explanation in the present work. This is equivalent to take the contact angle equal to 90° so that the surface is neither hydrophobic nor hydrophilic. In Section 4.5, the effect of variation of G_s on boiling will be investigated.

The gravitational force is expressed as [30]

$$\mathbf{F}_g = (\rho-\rho_{\text{ave}})\mathbf{g} \tag{12}$$

with $\mathbf{g}$ is the gravitational acceleration and ρ_{ave} is the average fluid density of the entire domain. With Eq. (12), the mass average velocity of the system keeps constant since a zero external force averaged in the entire domain.

After the collision step in momentum space, $\mathbf{m}^*$ is transformed back to the velocity space with $\mathbf{f}^* = \mathbf{T}^{-1}\mathbf{m}^*$ and then streamed with the following equation

$$f_\alpha(\boldsymbol{x}+\boldsymbol{e}_\alpha\delta t, t+\delta t) = f_\alpha^*(\boldsymbol{x},t) \tag{13}$$

The hydrodynamic field variables such as the density ρ and velocity $\mathbf{u}$ can be obtained from the first and second moments of the density distribution functions as follows:

$$\rho = \sum_{\alpha=0}^{18} f_\alpha \tag{14}$$

$$\rho u_i = \sum_{\alpha=0}^{18} f_\alpha e_{\alpha i} + 0.5F_i\delta_t \tag{15}$$

2.2. The thermal LB model

The thermal model is derived based on the entropy balance equation neglecting the viscous dissipation, which is given by

$$\rho T\frac{\mathrm{d}s}{\mathrm{d}t} = \nabla\cdot(\lambda\nabla T) \tag{16}$$

where s is the entropy and λ is the thermal conductivity. Substituting the thermodynamic relation $T\mathrm{d}s = c_v\mathrm{d}T + T\left(\frac{\partial p}{\partial T}\right)_v\mathrm{d}v = c_v\mathrm{d}T - \frac{T}{\rho^2}\left(\frac{\partial p}{\partial T}\right)_\rho\mathrm{d}\rho$ to Eq. (16), one can obtain the following equation

$$\frac{\mathrm{d}T}{\mathrm{d}t} = \frac{1}{\rho c_v}\nabla\cdot(\lambda\nabla T) - \frac{T}{\rho c_v}\left(\frac{\partial p}{\partial T}\right)_\rho\nabla\cdot\mathbf{u} \tag{17}$$

where c_v is the specific heat at constant volume. The following equation can be derived from the left hand side of Eq. (17)

$$\frac{\mathrm{d}T}{\mathrm{d}t} = \frac{\partial T}{\partial t} + (\mathbf{u}\cdot\nabla)T = \frac{\partial T}{\partial t} + \nabla\cdot(\mathbf{u}T) - T\nabla\cdot\mathbf{u} \tag{18}$$

Substituting Eq. (18) to Eq. (17), we can obtain

$$\frac{\partial T}{\partial t} + \nabla\cdot(\mathbf{u}T) = \frac{1}{\rho c_v}\nabla\cdot(\lambda\nabla T) + T\left(1-\frac{1}{\rho c_v}\right)\left(\frac{\partial p}{\partial T}\right)_\rho\nabla\cdot\mathbf{u} \tag{19}$$

It should be noted that the heat capacitance in the liquid–vapor–solid system varies greatly due to the large difference in heat capacity c_v or the density ρ. Therefore, the first term in the right hand side of Eq. (19) cannot be simplified as $\nabla\cdot(\chi\nabla T)$, in which $\chi = \lambda/\rho c_v$ is the thermal diffusivity. It is because of the discrepancy of heat capacitance that the conjugated heat exists in the system. For steady state, the heat capacitance can be assumed the same to simplify the treatment of the conjugated heat transfer. To introduce the treatment of conjugated heat transfer, Eq. (19) can be further transformed as

$$\begin{aligned} &\tfrac{\partial T}{\partial t} + \nabla\cdot(\mathbf{u}T) = \nabla\cdot(\chi\nabla T) + \varphi \\ &\varphi = -\nabla\left(\tfrac{1}{\rho c_v}\right)\cdot(\lambda\nabla T) + T\left(1-\tfrac{1}{\rho c_v}\right)\left(\tfrac{\partial p}{\partial T}\right)_\rho\nabla\cdot\mathbf{u} \end{aligned} \tag{20}$$

where the right-side first term of the source term φ comes from the following transformation:

$$\frac{1}{\rho c_v}\nabla\cdot(\lambda\nabla T) = \nabla\cdot(\chi\nabla T) - \nabla\left(\frac{1}{\rho c_v}\right)\cdot(\lambda\nabla T)$$

and it can be called as conjugated heat since only when the temperature in both fluid and solid should be simultaneously solved (conjugated) this term will play a role. The treatment of the conjugated heat in Eq. (20) is one-sided finite-difference approximation described as follows [38]

$$\begin{aligned} (\rho c_v)_{\text{avg}} &= \frac{(\rho c_v)_k + (\rho c_v)_{k+1}}{2},\ \frac{\partial}{\partial x_j}\left(\frac{1}{\rho c_v}\right)_k \\ &= \frac{(1/\rho c_v)_k - (1/\rho c_v)_{\text{avg}}}{\delta_j/2} \end{aligned} \tag{21}$$

where the average heat capacitance at the center point $(\rho c_v)_{\text{avg}}$ is obtained by the values of nodes k and $k+1$ and δ_j is the lattice space in j direction.

In order to solve the energy equation of Eq. (20), a thermal LB model is adopted

$$h_\alpha(\boldsymbol{x}+\boldsymbol{e}_\alpha\delta t, t+\delta t) = h_\alpha(\boldsymbol{x},t) - \frac{1}{\tau_T}\left(h_\alpha(\boldsymbol{x},t) - h_\alpha^{eq}(\boldsymbol{x},t)\right) + \omega_\alpha\varphi \tag{22}$$

where h_α ($\boldsymbol{x}$, t) is the temperature distribution function, φ is the source term and τ_T is the dimensionless relaxation time with $\tau_T = 0.5 + 3\chi\delta_t/\delta_x^2$. The equilibrium temperature distribution function is given by

$$h_\alpha^{eq}(\boldsymbol{x},t) = \omega_\alpha T\left(1 + \frac{3}{c^2}(\boldsymbol{e}_\alpha \cdot \mathbf{u}) + \frac{9}{2c^4}(\boldsymbol{e}_\alpha \cdot \mathbf{u})^2 - \frac{3}{2c^2}\mathbf{u}^2\right) \quad (23)$$

By using the Chapman-Enskog expansion, the thermal lattice model can retrieve Eq. (20) with $T = \sum_{\alpha=0}^{18} h_\alpha$.

3. Validation of code and boundary conditions

3.1. Code validation

Two representative problems are simulated to validate the present model. One is the evaluation of the Laplace law, and the other is the comparison of the coexistence curves between the numerical and theoretical curves predicted by the Maxwell equal-area construction.

For the first problem, a stationary droplet surrounded by vapor in a periodic zone with a mesh system of $201 \times 201 \times 201$ is adopted. The mesh resolution is 10 μm, and the real critical parameters of water are $\rho_{c,r} = 322\ \mathrm{kg\ m^{-3}}$, $T_{c,r} = 647.1$ K, $p_{c,r} = 22.064$ MPa. The conversion between the real property and the lattice property can be easily implemented according to the law of corresponding states. The Laplace law $\Delta p = 2\sigma/r$, in which σ is the surface tension and Δp is the pressure drop, is tested by varying the bubble radius r for a set of saturation temperature T_s. As shown in Fig. 1, the pressure drop varies linearly with $1/r$ for all the cases studied, and a comparison of surface tension predicted with the present model and the NIST data is listed in Table 1. The result shows a good match with the maximum deviation around 8%.

For the second problem, a stationary droplet with $r = 30$ (lattice unit) is initially placed in a periodic domain filled with vapor with a mesh system of $201 \times 201 \times 201$. The density of the droplet is slightly larger than ρ_c while the density of the vapor is slightly lower than ρ_c. By varying the saturation temperature T_s, densities of the vapor and liquid would finally reach the corresponding values. Fig. 2 shows the comparison of the coexistence curve obtained with the present model and the analytical result given by Maxwell construction. The result shows that thermodynamic consistency can be achieved well with the present model.

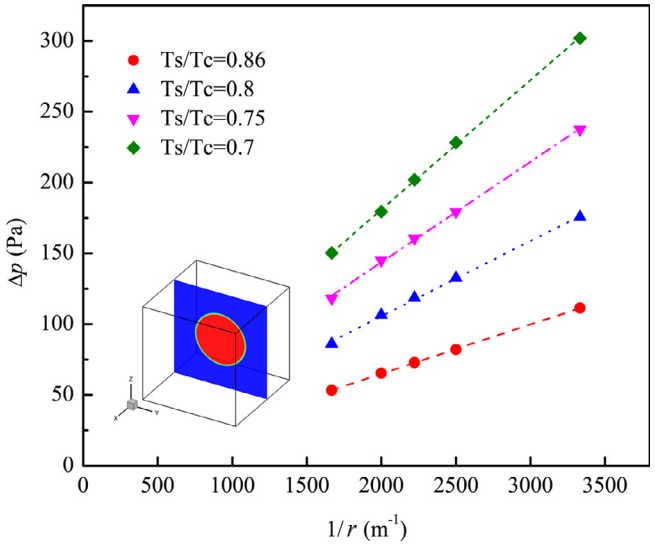

Fig. 1. Evaluation of the Laplace's law with the present model.

Table 1
Comparison of the surface tension obtained with the present model and NIST data.

T_s/T_c	σ (mN/m)		Deviation (%)
	Present model	NIST	
0.70	45.71	42.22	8.27
0.75	35.49	34.95	1.55
0.80	26.57	27.25	2.51
0.86	17.38	18.32	5.13

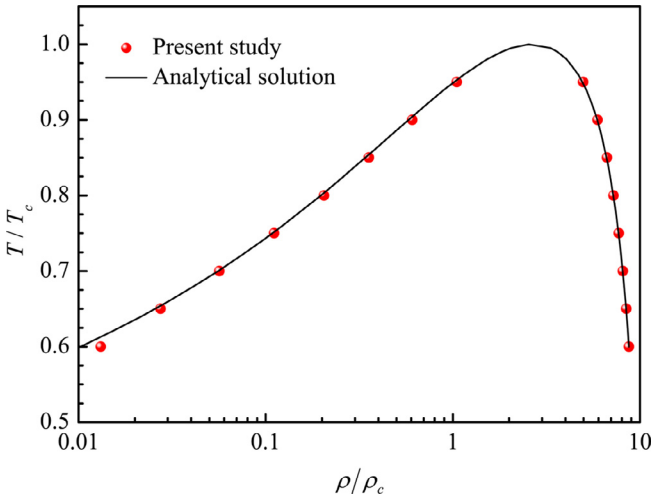

Fig. 2. Comparison of the coexistence curve obtained with the present model and the analytical solutions given by Maxwell construction.

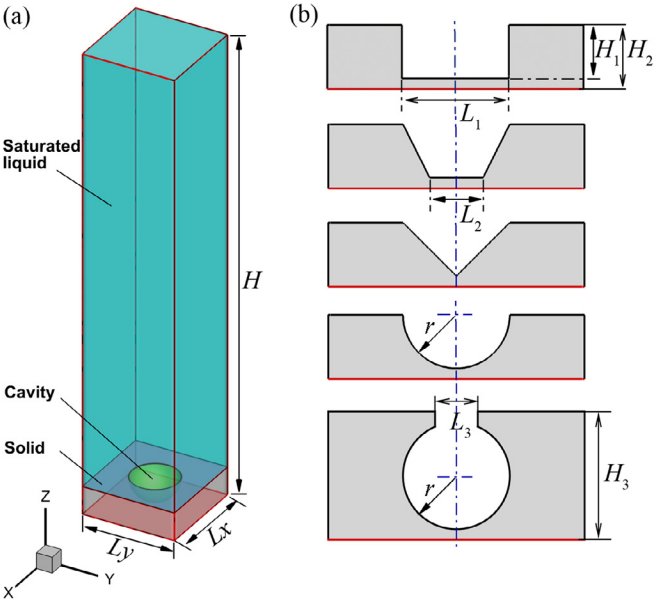

Fig. 3. Computational domain of the roughened surface with different kinds of cavities, (a) computational domain; (b) five different three dimensional cavities (For the first three cavities in both $x-z$ and $y-z$ directions, the cross-sections are rectangular, trapezoid and triangular, respectively; the fourth is spherical and the fifth is spherical reentrant).

3.2. Computational domain and boundary conditions

Simulations are performed on an open system filled with saturated water, and the water is heated through a solid with roughened surface. Fig. 3 depicts the cross-sections of five different three dimensional cavity grooves on the surface, namely the rectangular, trapezoidal and triangular in both $x-z$ and $y-z$

Table 2
Corresponding properties adopted in the simulation (lattice units).

	Liquid	Vapor	Solid
Density (ρ)	6.50	0.38	13.00
Kinetic viscosity (v)	0.08	0.35	–
Heat capacity (c_v)	9.33	8.42	2.45
Heat conductivity (λ)	3.57	0.44	3.51

directions, spherical and spherical reentrant ones. The geometries are chosen with simplicity and repeatability considered. The entire computational size $L_x \times L_y \times L_z$ is $1.2 \times 1.2 \times 6$ mm discretized by $120 \times 120 \times 600$ with the mesh resolution of 10 μm. The sizes of the cavity width L_1, L_2 and the thickness of the solid H_2, H_3 and the radius r are all kept as a constant throughout the simulation, and their values are 0.5, 0.25, 0.3, 0.6 and 0.25 mm, respectively. Without explicit explanation, the cavity height $H_1 = 0.25$ mm. The cavity mouth diameter L_3 of the reentrant cavities varies from 0.3 to 0.5 mm.

The temperature of the saturated water is initially set as $0.86\,T_c$, and all the corresponding properties for the two-phase together with the solid are listed in Table 2. Gravity is chosen as -2.5×10^{-5} in lattice unit. It is noted that the heat capacitance ratio between the liquid and vapor is 18.95. The viscosity ratio between the liquid and vapor is 3.91. The properties ζ (such as the heat capacity, kinetic viscosity and thermal diffusivity) at the two-phase interface are calculated with the following equation

$$\zeta = \frac{\rho_l - \rho}{\rho_l - \rho_g}\xi_l + \frac{\rho - \rho_g}{\rho_l - \rho_g}\xi_g \tag{24}$$

where the subscripts l and g denote liquid and vapor, respectively.

The detailed boundary conditions are as follows: the periodic boundary condition is applied at all the four lateral sides of the domain; convective boundary condition is defined at the outlet [46] and constant temperature T_c is set on the bottom of the solid. The LB model has intrinsic linear scalability in parallel computing, because the collision are calculated locally. It only takes about 5–6 h for one case with 100 CPU cores.

4. Results and discussion

In the following discussion, characterization of the nuclei growth and the whole bubble ebullition process will be firstly demonstrated; then the effect of cavity mouth on the nucleate boiling is performed on the reentrant cavities; finally, the effects of the solid thickness, surface wettability and base area on the nucleate boiling are explored for the rectangular cavities.

4.1. Characterization of vapor embryo formation

Heat is transferred by the transient conduction from the bottom of the solid to the liquid. It is expected that vapor embryo will be formed in the cavities due to the localized over-heating of liquid. Those liquid near the bottom of the cavities can obtain the heat firstly, and the superheated liquid turns to be lighter and becomes unstable according to the thermodynamic equation of state. Consequently, generation of a bubble embryo becomes probable. This phenomenon has been observed in a large number of experimental works using high-speed photography [8,11,12]. Fig. 4 presents the snapshots of the nucleation embryos under different cavities. It shows that the vapor embryos are generated from the cavities. It

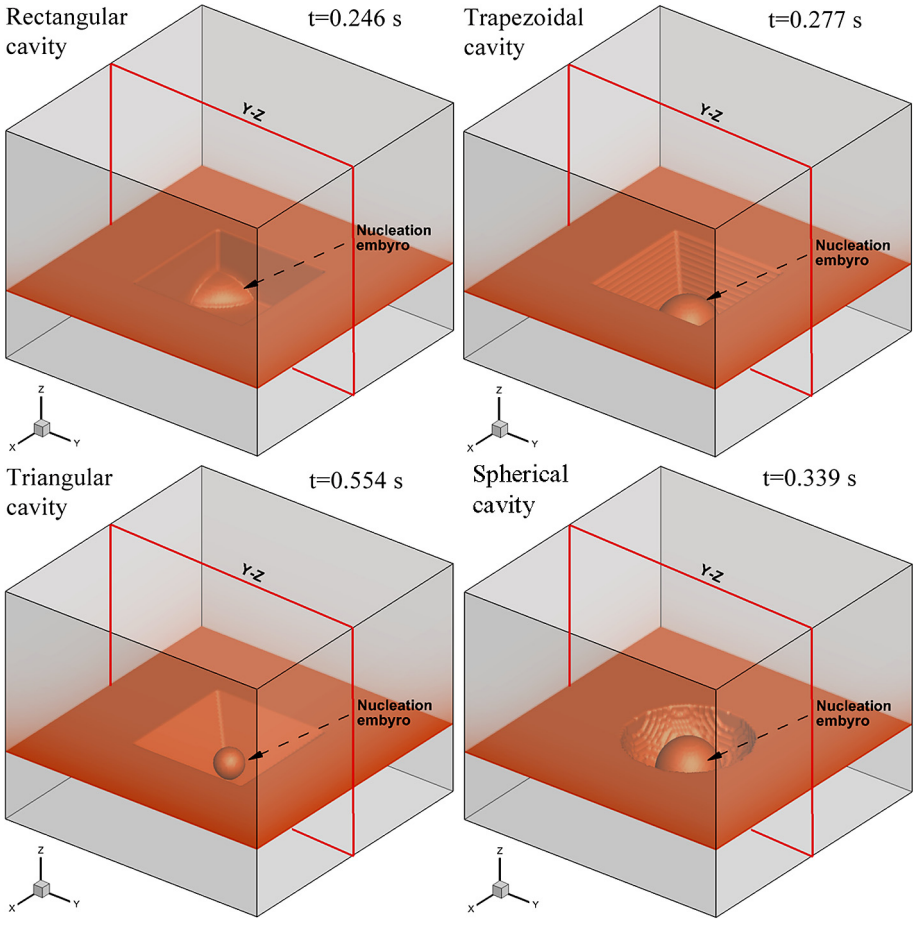

Fig. 4. Snapshots of bubble embryo nucleation emerged from the roughened surface with different cavities.

is noted that the radius size of the nucleation embryo is numerically predicted around 10 lattices (100 μm), while the typical width of the diffuse interface is around 4–5 lattices (40–50 μm). Besides, the density ratio we choose is not large and can also minimize the influence of the diffusion width. The result is consistent with the classical nucleation theories that the interfacial free energy of the nucleation can be lowered for an embryo in a cavity of a solid [3]. It can also be observed that the embryos in all the cavities except the rectangular cavity are somewhat spherical and the embryos tend to be generated at the center regions of the cavities firstly. Similar results have also been numerically reported by Gong et al. [47] and experimentally reported by Kandlikar [11] who indented a small fin in the heater surface and observed the preference of nucleation occurring on the sharp corner.

To better reveal the evolution process of the nucleation embryos formatted from the corners, the Y-Z cross-section (x = 0.6 mm) has been chosen and the snapshots of density distributions of different cavities are presented in Fig. 5. Attention is firstly turned to the rectangular cavity. It can be found clearly that unlike the other cavities where the embryos generate at the middle position, the embryo forms at the lateral sides of the rectangular cavity. Since the thermal diffusivity of the solid is larger than that of the liquid, the temperature of the lateral walls (acting as fins) of the cavity thereby is higher than that of the bulk liquid near the cavity bottom. Therefore, the rectangular cavity benefits the heat transfer of the liquid at the sharp corners and promotes the nucleation. The bubble trajectory during its growth is below 45° angle and tends to be horizontal. This phenomenon is attributed to the evaporation momentum force acting on the vapor. Evaporation at the liquid–vapor interface can result in a force when the momentum of the vapor phase leaves the interface [11]. A schematic illustration on the phenomenon is depicted in Fig. 6. For a bubble motion on the horizontal heated surfaces (see Fig. 6(a)), the evaporation momentum forces in the x-direction, $F_{m,1x}$ and $F_{m,2x}$ can cancel each other if the heater surface temperature T_1 equals T_2, and the bubble departure is determined by the vertical forces. If T_1 is larger than T_2, the evaporation rate on the right surface is larger and results in a positive force in the x-direction. Similar for a bubble motion at the sharp corner (see Fig. 6(b)), the temperature of the lateral wall T_2 is lower than that of the bottom wall T_1 due to a larger heat conduction resistance. The direction of the net momentum $F_{m,total}$ thereby is in an angle below 45° angle.

It can also be found in Fig. 5 that the time needed for the nucleation of triangular cavity is the longest. This is mainly because of the cavity shape: the triangular cavity is occupied by the least liquid and only a small part of the liquid can obtain the heat due to its smallest contact area with the solid (bottom area of the cavity). Compared with the spherical cavity, the contact area of the trapezoidal cavity is much larger, and therefore a larger volume of the vapor is generated at t = 0.277 s. In summary, a larger bottom area of the cavity is beneficial for the nucleation embryo formation.

4.2. Bubble dynamics on roughened surfaces

It is widely recognized that the boiling heat transfer is mainly from three mechanisms, namely, transient conduction, microconvection and micro-layer evaporation. A schematic illustration

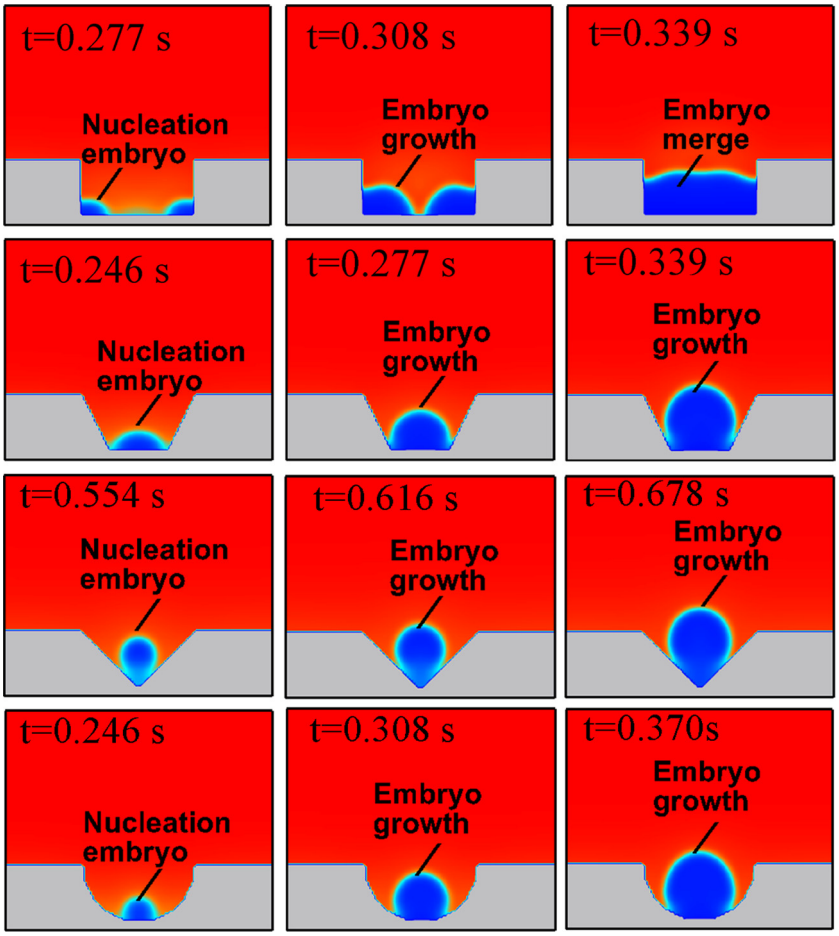

Fig. 5. Evolution of the nucleation embryo in different cavities at the Y-Z cross-section.

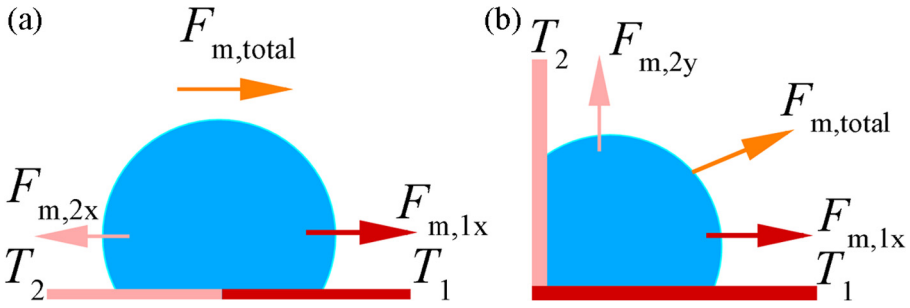

Fig. 6. Schematic illustrations of the evaporation momentum forces determining the embryo growth, (a) interfaces with different overheat; (b) cavity corner.

of the heat transfer mechanisms during the bubble nucleation process is depicted in Fig. 7. Transient conduction (Q_{tc}) into the fluid mainly involves the micro-layer liquid trapped underneath the vapor and the liquid attached to the heating surface, and only a comparatively small part conducts to the vapor due to its low conductivity. The bubble grows through the evaporation of the three-phase contact line (Q_{cl}) and the superheated liquid surrounding the vapor (Q_{lv}). The continuous growth and departure of the bubble promotes the micro-convection heat transfer (Q_{mc}) and the natural convection (Q_{nc}) due to the disruption of boundary layer. Recent experimental work [5,11] demonstrated that the dominant mechanism by which heat is transferred is through transient conduction and micro-convection, while that through micro-layer evaporation and contact line is less than 25%.

Fig. 8 presents the time evolution of the total heat transfer rate on the heating surface with different cavities. The local heat flux q and total heat transfer rate Q on the bottom surface area of the solid (A) are defined as follows:

$$q = \lambda_s \left(\frac{\partial T}{\partial z}\right)_{z=0}, \quad Q = \iint_A q \mathrm{dA} \tag{25}$$

It can be found that a slight variation trend of the total heat transfer rate occurs at "A" due to the occurrence of the nucleation, which is consistent with the results presented in Section 4.1. Before the nucleation happens, the heat transfer performance with rectangular cavity is the best while that with the triangular cavity is the worst. The total volume of the solid for the rectangular cavity is the smallest, hence, at the same bottom surface temperature the rectangular cavity surface has a higher temperature compared with other cavities which is beneficial to nucleation. As time proceeds, the temperature difference between the heating surface and the fluid decreases, resulting in a decreasing tendency of the total heat transfer on the whole. Unlike the plain plate, micro-convection for the constrained cavities is weakened since the cavities are occupied by the vapor and little liquid rewets the heating surface. Therefore the heat for the vapor growth mainly depends on the heat obtained from its surrounding liquid (Q_{lv}). For the first several bubble ebullition cycles, the temperature of the liquid surrounding the vapor is low and gradually increases with time, and therefore the nucleation characteristics in terms of the departure period and the amplitude of the total heat transfer rate vary with time. After that, the total heat transfer rate reaches a relatively steady state with the increase in temperature of the superheated liquid. The right-upper corner picture of Fig. 8 gives magnified variation trends.

Fig. 9 shows the dimensionless heat transfer rate and bubble dynamics for different cavities. The dimensionless heat transfer rate is defined as

$$Q' = \frac{Q - Q_{min}}{Q_{max} - Q_{min}} \tag{26}$$

where Q_{min} and Q_{max} are the minimum and maximum total heat transfer rate in one bubble ebullition cycle under steady regime.

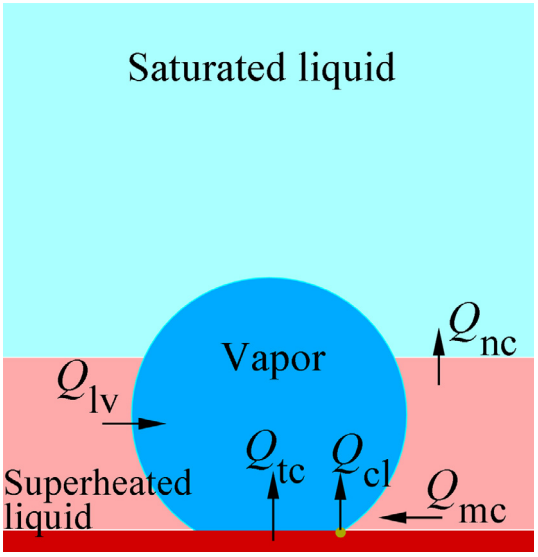

Fig. 7. Schematic illustration of the heat transfer mechanisms during the bubble nucleation process.

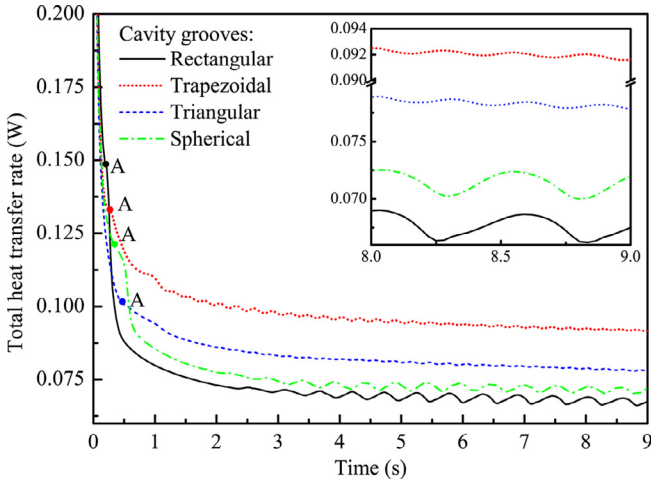

Fig. 8. Time evolution of the total heat transfer rate on the heating surface with different cavities.

The dimensionless time for the moment of a bubble departure is referred as 0 in Fig. 9(a) and (b), where dT denotes the dimensionless period time. It can be found that the dimensionless heat transfer rate at t = 0 dT is nearly the lowest. After that, liquid flushes as the bubble departs which results in an enhanced convective heat transfer and thereby an increasing heat flux. The table imbedded

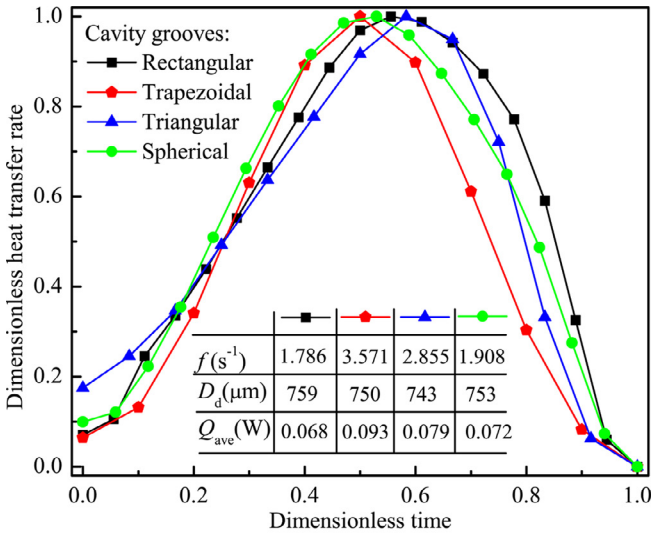

(a) Dimensionless heat transfer rate

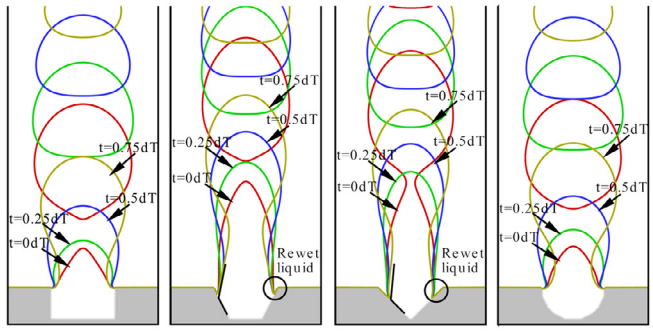

(b) Bubble dynamics

Fig. 9. Dimensionless heat transfer rate and bubble dynamics in a typical ebullition cycle for different cavities, (a) dimensionless heat transfer rate; (b) bubble dynamics.

in Fig. 9(a) shows that the trapezoidal and triangular cavities perform much better in terms of the release frequency f and the average heat transfer rate Q_{ave}. The release frequencies for the rectangular, trapezoidal, triangular and spherical cavities are 1.786, 3.571, 2.855 and 1.908 s^{-1} and the average heat transfer rates over the whole heating area in one ebullition period are 0.068, 0.093, 0.079 and 0.072 W, respectively.

Attention is now turned to the bubble release frequency, which is related to the bubble diameter at departure, bubble growth rate and the heat transfer into and out of the bubble. Regarding to the release frequency of cavities, it is essential to focus on the mechanism of the stability of the gas entrapment in cavities. Anderson and Mudawar [48] experimentally studied various cavities on the boiling of saturated FC-72 and concluded that the drilled cavities were ineffective to maintain stable vapor embryo. Here drilled cavities refer to those shapes having tilted lateral surface, such as triangular and trapezoidal cavities. The experimental result is consistent with the present result that the release frequency of the trapezoidal and triangular cavities is higher. Besides, a higher average total heat transfer rate and a larger bubble neck after the departure of the former bubbles are beneficial for the bubble departure. Generally speaking, a higher release frequency corresponds to a relatively smaller bubble departure diameter as shown in Fig. 9(a). Fig. 9(b) presents a straightforward illustration of the bubble ebullition cycle with the Y-Z cross-section chosen. It can be seen that the cavity mouths of the trapezoidal and triangular cavities are not fully occupied compared with the other two cavities, which result in a larger solid surface area exposure in the liquid. Rewetting liquid tends to take more heat from the surface. For the spherical and rectangular cavities, the performance of the surface with spherical cavity is slightly better in terms of the bubble release frequency and average heat transfer rate, which may be due to its less capability in trapping the vapor caused by its inherent structure. Similar result has been confirmed by the experimental work conducted by Das et al. [20].

Fig. 10 presents the local heat flux snapshots on the heating surface at t = 0, 0.25 and 0.5 dT, where Figs. 10(a–d) correspond to the rectangular, trapezoidal, triangular and spherical cavities, respectively. Fig. 10(e) represents the experimentally measured local heat flux by Wagner and Stephan [49] who tested the local heat flux for single bubble event at a single nucleation site. It can be found that the central region underneath the cavity mouth is relatively small for all the four cavities. For the rectangular cavity, the lowest local heat flux occurs at the four corners where more vapor exists as is stated before. For the trapezoidal cavity, the local heat flux beneath the cavity bottom is relatively lower and the highest heat flux exists right at the four corners. For the triangular and spherical cavities, the local heat flux increases firstly and then radially decreases and decreases, respectively. Such distribution features of the local heat flux qualitatively agree well with the experimental work shown in Fig. 10(e).

4.3. Effect of cavity mouth on the nucleation boiling heat transfer

Experimental studies indicate that cavity mouth determines the superheat needed for the bubble nucleation. According to the heterogeneous nucleation theory, the superheat at boiling incipience ΔT for a bubble resting in a cavity is written as [14]

$$\Delta T = \frac{q d_{eq}}{2\lambda_l} + \frac{T_{sat}(v_g - v_l)}{h_{lg}}\left(\frac{4\sigma}{d_{eq}} - p_{gb}\right) \tag{27}$$

where q is the heat flux, v_l and v_g are the specific volumes of liquid and gas, h_{lg} is the latent heat, p_{gb} is the partial gas pressure in the bubble, d_{eq} refers to the equivalent cavity mouth diameter. The first term in Eq. (27) is comparatively smaller than the second term, and therefore the superheat temperature required decreases with the cavity mouth.

By varying the cavity mouth L_3 from 300 to 500 μm, the influence of the cavity mouth of the reentrant cavities on the NBHT is investigated. Fig. 11 illustrates the time evolution of the total heat transfer rate of the heating surface. Compared with the four cavities studied before, the total heat transfer rate with reentrant cavities is relatively small, which is attributed to a larger volume of the solid surrounding the cavity (see Fig. 3). As is seen from the inserted magnified figure in Fig. 11, the total heat transfer rate increases with the cavity mouth during the time of 0–0.5 s and then decreases during the time of 0.5–1.5 s. This phenomenon could be explained as follow. No nucleation occurs for all of the reentrant cavities before the time of 0.5 s. As the cavity mouth increases, at given L_x and L_y the volume of the solid decreases which benefits the heat transfer from the heating surface to the liquid in the cavity. After a certain time period before 1.5 s, vapor embryos are firstly generated in the reentrant cavity with the mouth of 500 μm, resulting in a decreasing total heat transfer rate since the bottom of the cavity is occupied by the vapor. Beyond about 1.5 s the three cavities are all occupied by vapor, and then cavity with a larger mouth once again receives more heat because of its less wall conduction resistance and larger three-phase contact line.

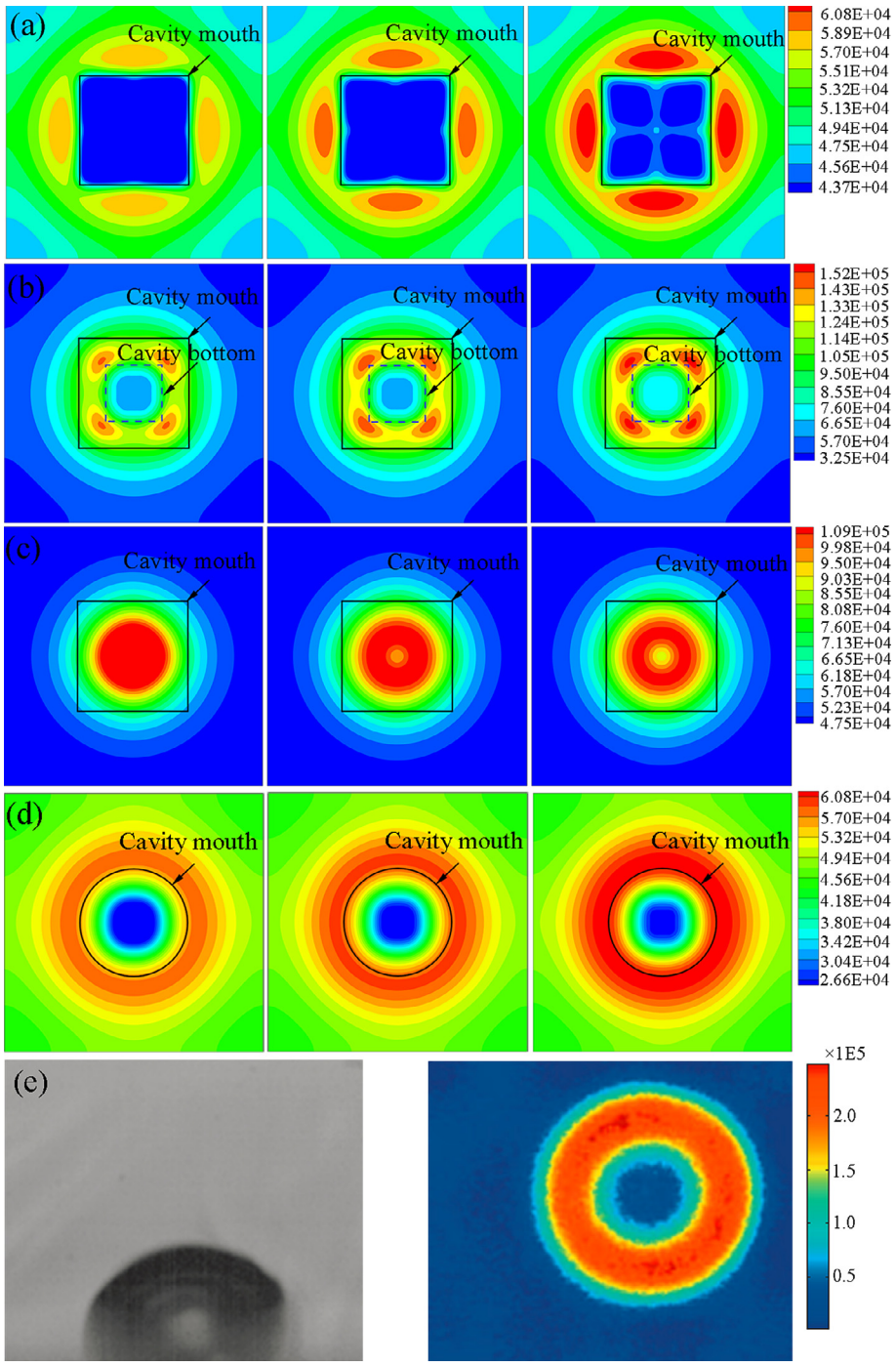

Fig. 10. Local heat flux snapshots on the heating surface at $t = 0$, 0.25 and 0.5 dT (unit: W m^{-2}), (a) rectangular cavity; (b) Trapezoidal cavity, (c) triangular cavity; (d) spherical cavity; (e) experimental snapshot produced from Wagner and Stephan [49].

The bubble ebullition processes of the three reentrant cavities are depicted in Fig. 12. The perimeter of the cavity mouth serves as the three-phase contact line. As the cavity mouth increases, the increasing perimeter of the three-phase contact line and decreasing conduction resistance enhance the average heat transfer rate on the cavity surface. The result is consistent with Eq. (27) that a larger cavity mouth needs a relative smaller superheat due to the heat transfer enhancement. In addition, a narrow cavity is considered to be easier to trap the bubble. Besides, the neck of the residual bubble increases with the cavity mouth, which results in a higher release frequency with the cavity mouth. For the given sizes and physical parameters, the bubble release frequencies for the cavity mouth of 300, 400 and 500 μm are 1.505, 1.613 and 1.615 s^{-1}, respectively. The bubble departure diameter also increases slightly with the cavity mouth, because a larger wetted perimeter causes a larger surface stress which could resist the buoyancy force acting on the bubble for its departure.

4.4. Effect of wall thickness on the nucleation boiling heat transfer

The thickness of the solid, together with the cavity/fin height, determines the conductance of the transient heat conduction. To better understand the influence of the solid thickness on the NBHT, three rectangular cavities are chosen with different solid thickness.

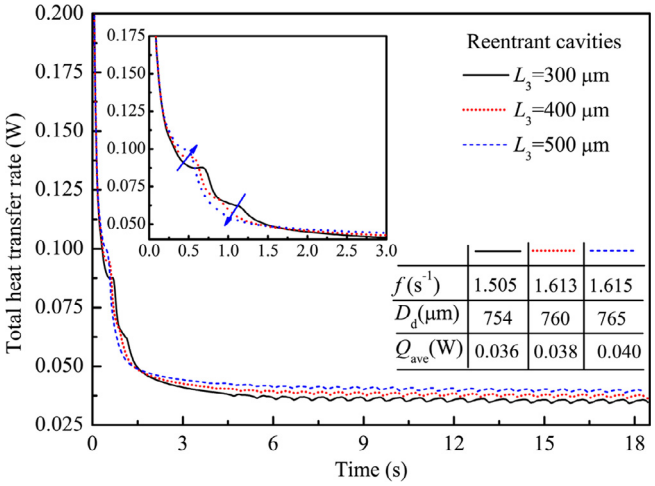

Fig. 11. Time evolution of the total heat flux on the heating surface with different cavity mouths for reentrant cavity.

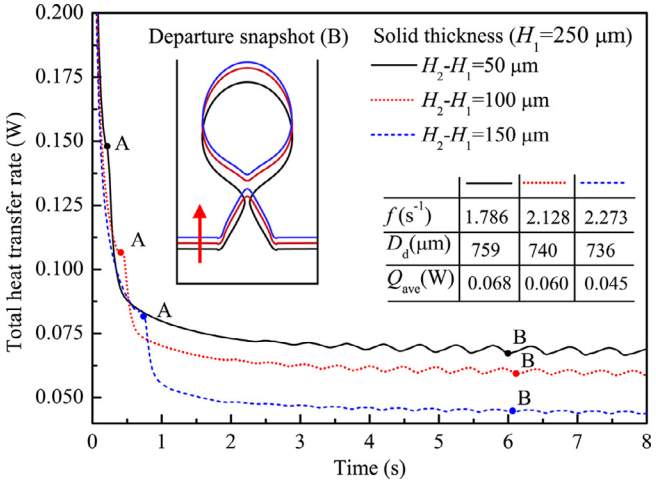

Fig. 13. Influences of the solid thicknesses on the NBHT for the rectangular cavity.

Fig. 13 presents the time evolution of the total heat transfer rate of the three cavities. As is expected, transient conduction resistance decreases rapidly with a thinner solid thickness and thereby promotes the occurrence of nucleation. The average total heat transfer rate for the thickness equaling 50, 100 and 150 μm are 0.068, 0.060 and 0.045 W, respectively. For the cases studied the total heat transfer resistance is composed of two parts: wall conduction resistance and surface convective resistance. When the thickness is lower than 100 μm the conduction resistance is not dominant, while beyond 100 μm, it may be the major part of the total resistance, leading to a significant reduction of heat transfer rate from 100 to 150 μm. This phenomenon has also been observed by Magrini and Nannei [50] who conducted pool boiling of water with different kinds of solid materials of different thickness. Their results suggested that the effect of thickness on HTC became negligible at some limiting values, and the values differ greatly for different solid materials. With the increase of the thickness, the conduction resistance dominates and the total heat transfer rate decreases greatly. The bubble departure diameter decreases slightly with the increase in solid wall thickness.

4.5. Effect of wettability on the nucleation boiling heat transfer

By varying G_s in Eq. (11), either a hydrophilic surface (say contact angle θ of 70°) or a hydrophobic surface (say contact angle θ of 120°) can be obtained. The total heat transfer rate on the heating surface with different contact angles are depicted in Fig. 14. As is shown in Fig. 14(a) nucleation occurs easily on the surface with low wettability, i.e. hydrophobic surface. The locations where the vapor embryos are generated are quite different for the surfaces with different contact angles. For the hydrophobic surface vapor embryos occur at the cavity corners and form a concave surface. While for the hydrophilic surface, the nucleation occurs near the cavity corners and forms a convex surface. One possible reason may be as follows. On the hydrophilic surface, liquid tends to flood the dry-out area once embryos are generated, and then expels the embryos moving away from the cavity lateral wall.

As is shown in Fig. 14(b), the total heat transfer rates for the contact angles of 70°, 90° and 120° are 0.067, 0.068 and 0.072 W, respectively. It indicates that the nucleate boiling heat transfer can be enhanced by reducing surface wettability.

4.6. Effect of cavity base area on the nucleation boiling heat transfer

By varying the length of the solid $L_{x,y}$ while keeping the cavity mouth constant, the influence of the cavity base area is studied. Fig. 15 presents the time evolution of the total heat transfer on the heating surface with different cavity base area (shown by its one side length). As is expected, the total heat transfer rate increases with the cavity base area. The average total heat transfer

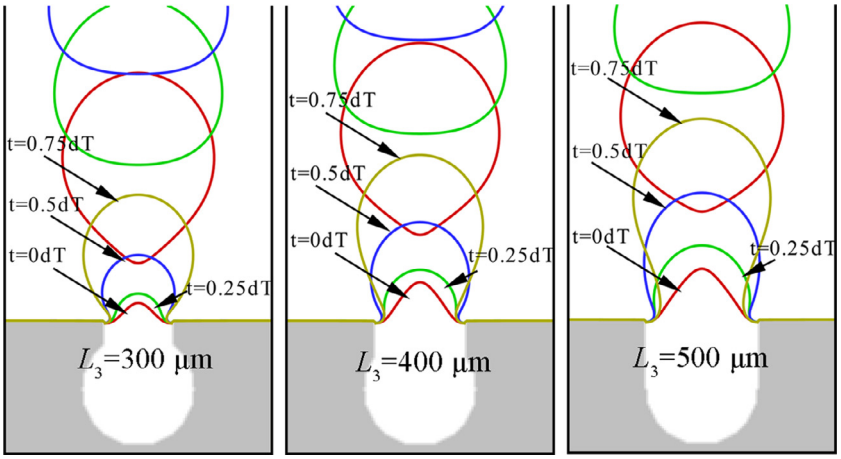

Fig. 12. Bubble dynamics of the reentrant cavity with different cavity mouths.

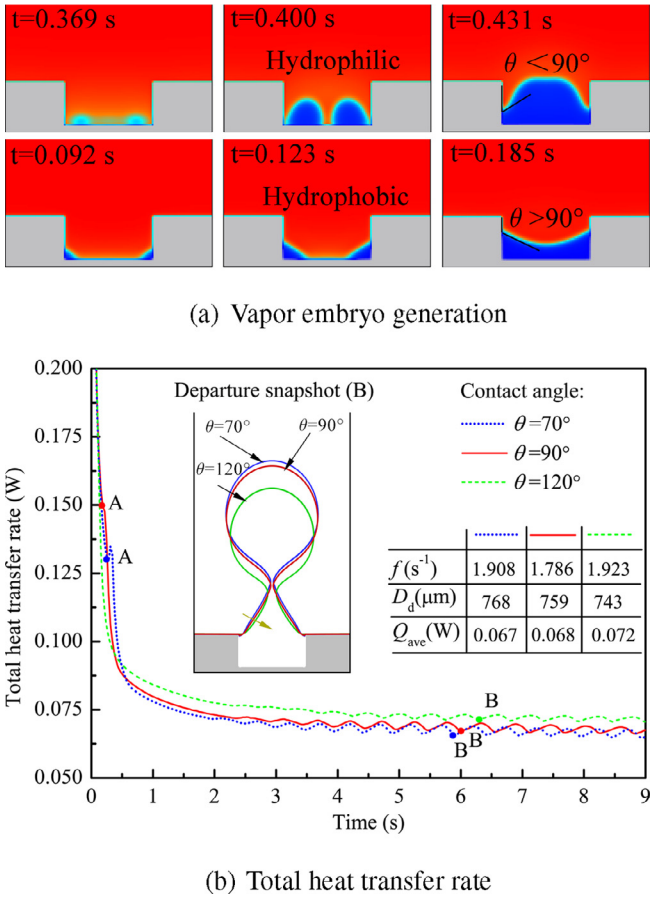

Fig. 14. Influences of the contact angle on the NBHT for the rectangular cavity, (a) vapor embryo generation; (b) total heat transfer rate.

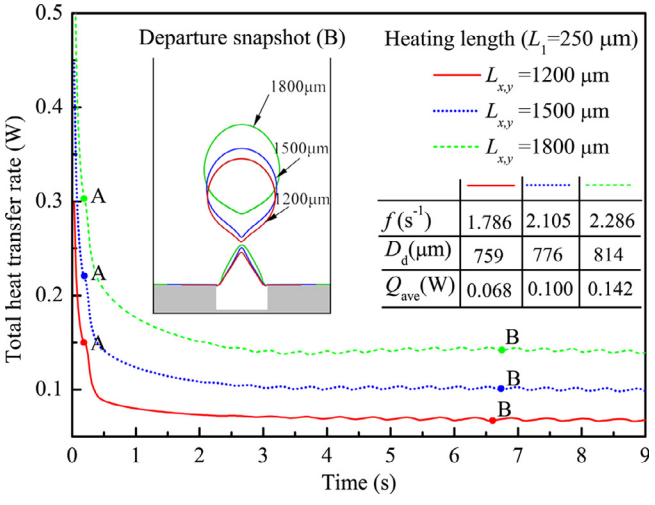

Fig. 15. Influences of the cavity base area on the NBHT for the rectangular cavity.

rate for the three heater lengths of 1200, 1500 and 1800 μm are 0.068, 0.100 and 0.142 W, respectively. While the average values of the heat flux are 4.72, 4.44 and 4.38 $\times$ 10^4 W m^{-2}, respectively. The bubble release frequency increases with the cavity base area since more heat is transferred to the vapor. Departure diameter shown in the inserted figure suggests that a larger departure diameter should be achieved because more heat can be taken away from a larger base area.

5. Conclusions

A three-dimensional phase change model with conjugated heat transfer among the liquid–vapor–solid has been proposed and applied to the entire bubble ebullition cycle on five types of roughened surfaces at meso-scale level by multi-relaxation lattice Boltzmann method. The main results are as follows:

1. Nucleation process, i.e., the generation and growth of a nuclei, is obtained without introducing any artificial input; the nucleation for the rectangular cavity locates at the corners which is quite different from the other cavities where the embryos generate at the center of the cavities; a larger bottom area of a cavity benefits for the occurrence of the nucleation.
2. Cavity mouths with trapezoidal and triangular cavities are not fully occupied by the residual vapor, and an improvement of the total heat transfer rate is observed; the bubble release frequencies for these two cavities are relatively higher than the spherical and rectangular cavities.
3. For the reentrant cavity the total heat transfer rate increases with a larger cavity mouth due to a larger perimeter of the three-phase contact line.
4. A critical value (100 μm in the present work) for the solid thickness exists beyond which the total heat transfer rate decreases greatly due to the predominance of the conduction resistance.
5. Surface with low wettability can improve the bubble release frequency.
6. Cavity base area promotes the bubble nucleation because more heat can be absorbed by the bubble, but results in a low power density on the heating surface.

Finally it should be noted that the density ratio adopted in this paper is only 17. Further research is highly needed to extend the density ratio of liquid over vapor while still keeping numerical stability.

Acknowledgement

This work is supported by the Key Project of the National Natural Science Foundation of China (51136004) and (51406145).

References

[1] D.E. Kim, D.I. Yu, D.W. Jerng, M.H. Kim, H.S. Ahn, Review of boiling heat transfer enhancement on micro/nanostructured surfaces, Exp. Thermal Fluid Sci. 66 (2015) 173–196.
[2] I.L. Pioro, W. Rohsenow, S.S. Doerffer, Nucleate pool-boiling heat transfer. I: review of parametric effects of boiling surface, Int. J. Heat Mass Transfer 47 (23) (2004) 5033–5044.
[3] S.F. Jones, G.M. Evans, K.P. Galvin, Bubble nucleation from gas cavities – a review, Adv. Colloid Interface Sci. 80 (1999) 27–50.
[4] T.G. Theofanous, J.P. Tu, A.T. Dinh, T.N. Dinh, The boiling crisis phenomenon Part I: nucleation and nucleate boiling heat transfer, Exp. Thermal Fluid Sci. 26 (2002) 775–792.
[5] J. Kim, Review of nucleate pool boiling bubble heat transfer mechanisms, Int. J. Multiph. Flow 35 (12) (2009) 1067–1076.
[6] C.E. Brennen, Caviation and Bubble Dynamics, Cambridge University Press, New York, 2013.
[7] M.E. Poniewski, J.R. Thome, Nucleate Boiling on Micro-Structured Surfaces, Heat Transfer Research, Inc., 2008.
[8] D. Deng, J. Feng, Q. Huang, Y. Tang, Y. Lian, Pool boiling heat transfer of porous structures with reentrant cavities, Int. J. Heat Mass Transfer 99 (2016) 556–568.
[9] A.S. Moita, E. Teodori, A.L.N. Moreira, Influence of surface topography in the boiling mechanisms, Int. J. Heat Fluid Flow 52 (2015) 50–63.
[10] X. Quan, M. Gao, P. Cheng, J. Li, An experimental investigation of pool boiling heat transfer on smooth/rib surfaces under an electric field, Int. J. Heat Mass Transfer 85 (2015) 595–608.
[11] S.G. Kandlikar, Controlling bubble motion over heated surface through evaporation momentum force to enhance pool boiling heat transfer, Appl. Phys. Lett. 102 (5) (2013) 051611.

[12] H. Jo, S. Kim, H. Kim, J. Kim, M.H. Kim, Nucleate boiling performance on nano/microstructures with different wetting surfaces, Nanoscale Res. Lett. 7 (1) (2012) 242–250.
[13] A.K. Das, P.K. Das, P. Saha, Nucleate boiling of water from plain and structured surfaces, Exp. Thermal Fluid Sci. 31 (8) (2007) 967–977.
[14] H. Honda, J.J. Wei, Enhanced boiling heat transfer from electronic components by use of surface microstructures, Exp. Thermal Fluid Sci. 28 (2–3) (2004) 159–169.
[15] D. Wen, Influence of nanoparticles on boiling heat transfer, Appl. Therm. Eng. 41 (2012) 2–9.
[16] H. Kim, Enhancement of critical heat flux in nucleate boiling of nanofluids: a state-of-art review, Nanoscale Res. Lett. 6 (1) (2011) 415–432.
[17] M. Jakob, Heat transfer in evaporation and condensation-I, Mech. Eng. (Am. Soc. Mech. Eng.) 58 (1936) 643–660.
[18] J.D. Bernardin, I. Mudawar, A cavity activation and bubble growth model of the Leidenfrost point, J. Heat Transfer 124 (2002) 864–874.
[19] J.Y. Chang, S.M. You, Enhanced boiling heat transfer from micro-porous surfaces: effect of coating composition and method, Int. J. Heat Mass Transfer 40 (1997) 4449–4460.
[20] A.K. Das, P.K. Das, P. Saha, Performance of different structured surfaces in nucleate pool boiling, Appl. Therm. Eng. 29 (17–18) (2009) 3643–3653.
[21] K. Chu, R. Enright, E.N. Wang, Structured surfaces for enhanced pool boiling heat transfer, Appl. Phys. Lett. 100 (24) (2012) 241603.
[22] L. Dong, X. Quan, P. Cheng, An experimental investigation of enhanced pool boiling heat transfer from surfaces with micro/nano-structures, Int. J. Heat Mass Transfer 71 (2014) 189–196.
[23] R.L. Webb, The evolution of enhanced surface geometries for nucleate boiling, Heat Transfer Eng. 2 (3–4) (1981) 46–69.
[24] J.Y. Chang, S.M. You, Boiling heat transfer phenomena from micro-porous surfaces in saturated FC-72, Int. J. Heat Mass Transfer 40 (18) (1997) 4437–4447.
[25] V.V. Chekanov, Interaction of centers in nucleate boiling. High Temperature Thermo-physics (in Russian), 15 (1977) 121–128.
[26] L. Zhang, M. Shoji, Nucleation site interaction in pool boiling on the artificial surface, Int. J. Heat Mass Transfer 46 (3) (2003) 513–522.
[27] K. Ling, Z.Y. Li, W.Q. Tao, A direct numerical simulation for nucleate boiling by the VOSET method, Numer. Heat Transfer 65 (10) (2014) 949–971.
[28] H. Inaoka, N. Ito, Numerical simulation of pool boiling of a Lennard–Jones liquid, Physica A 392 (18) (2013) 3863–3868.
[29] Q. Li, K.H. Luo, Q.J. Kang, Y.L. He, Q. Chen, Q. Liu, Lattice Boltzmann methods for multiphase flow and phase-change heat transfer, Prog. Energy Combust. Sci. 52 (2016) 62–105.
[30] L. Chen, Q.J. Kang, Y.T. Mu, Y.L. He, W.Q. Tao, A critical review of the pseudopotential multiphase lattice Boltzmann model: methods and applications, Int. J. Heat Mass Transfer 76 (2014) 210–236.
[31] Q. Li, Q.J. Kang, M.M. Francois, Y.L. He, K.H. Luo, Lattice Boltzmann modeling of boiling heat transfer: the boiling curve and the effects of wettability, Int. J. Heat Mass Transfer 85 (2015) 787–796.
[32] S. Gong, P. Cheng, A lattice Boltzmann method for simulation of liquid-vapor phase-change heat transfer, Int. J. Heat Mass Transfer 55 (17–18) (2012) 4923–4927.
[33] A. Márkus, G. Házi, On pool boiling at microscale level: the effect of a cavity and heat conduction in the heated wall, Nucl. Eng. Des. 248 (2012) 238–247.
[34] A. Márkus, G. Házi, Numerical simulation of the detachment of bubbles from a rough surface at microscale level, Nucl. Eng. Des. 248 (2012) 263–269.
[35] R. Zhang, H. Chen, Lattice Boltzmann method for simulations of liquid–vapor thermal flows, Phys. Rev. E 67 (6) (2003) 066711.
[36] S. Gong, P. Cheng, Lattice Boltzmann simulations for surface wettability effects in saturated pool boiling heat transfer, Int. J. Heat Mass Transfer 85 (2015) 635–646.
[37] V.K. Dhir, Mechanistic prediction of nucleate boiling heat transfer – achievable or a hopeless task, ASME J. Heat Transfer 128 (2006) 1–12.
[38] H. Karani, C. Huber, Lattice Boltzmann formulation for conjugate heat transfer in heterogeneous media, Phys. Rev. E 91 (2) (2015) 023304.
[39] Y.T. Mu, L. Chen, Y.L. He, W.Q. Tao, Pore-scale modelling of dynamic interaction between SVOCs and airborne particles with lattice Boltzmann method, Build. Environ. 104 (2016) 152–161.
[40] Y.T. Mu, L. Chen, Y.L. He, W.Q. Tao, Coupling finite volume and lattice Boltzmann methods for pore scale investigation on volatile organic compounds emission process, Build. Environ. 92 (2015) 236–245.
[41] K.N. Premnath, J. Abraham, Three-dimensional multi-relaxation time (MRT) lattice-Boltzmann models for multiphase flow, J. Comput. Phys. 224 (2) (2007) 539–559.
[42] D. Zhang, K. Papadikis, S. Gu, Three-dimensional multi-relaxation time lattice-Boltzmann model for the drop impact on a dry surface at large density ratio, Int. J. Multiph. Flow 64 (2014) 11–18.
[43] T. Lee, C. Lin, A stable discretization of the lattice Boltzmann equation for simulation of incompressible two-phase flows at high density ratio, J. Comput. Phys. 206 (1) (2005) 16–47.
[44] Q. Li, K.H. Luo, X.J. Li, Lattice Boltzmann modeling of multiphase flows at large density ratio with an improved pseudopotential model, Phys. Rev. E 87 (5) (2013) 053301.
[45] P. Yuan, L. Schaefer, Equations of state in a lattice Boltzmann model, Phys. Fluids 18 (4) (2006) 042101.
[46] Q. Lou, Z. Guo, B. Shi, Evaluation of outflow boundary conditions for two-phase lattice Boltzmann equation, Phys. Rev. E 87 (6) (2013) 063301.
[47] S. Gong, P. Cheng, X. Quan, Two-dimensional mesoscale simulations of saturated pool boiling from rough surfaces. Part I: bubble nucleation in a single cavity at low superheats, Int. J. Heat Mass Transfer 100 (2016) 927–937.
[48] T.M. Anderson, I. Mudawar, Microelectronic cooling by enhanced pool boiling of a dielectric fluorocarbon liquid, J. Heat Transfer 111 (1989) 752–759.
[49] E. Wagner, P. Stephan, High-resolution measurements at nucleate boiling of pure FC-84 and FC-3284 and its binary mixtures, J. Heat Transfer 131 (12) (2009) 121008.
[50] U. Magrini, E. Nannei, On the influence of the thickness and thermal properties of heating walls on the heat transfer coefficients in nucleate pool boiling, J. Heat Transfer 97 (2) (1975) 173–178.